The Atmospheric Scale Lengths of Turbulence and Its Dependencies Derived from GPS Single Difference with a Common Clock

Gaël Kermarrec[1] and Steffen Schön[2]

[1]Geodetic Institute, Leibniz Universität Hannover, Nienburger Str. 1, 30167 Hannover, Germany

[2]Institut für Erdmessung, Leibniz University Hannover, Schneiderberg 50, 30167 Hannover, Germany

Corresponding author: Gaël Kermarrec (kermarrec@gih.uni-hannover.de)

Key Points:

- Signals from Global Navigation Satellite Systems are influenced by random variations of the refractivity index as they travel through the troposphere
- The power spectral density of positioning residuals from Single Differenced phase observations allows studying key parameters of tropospheric turbulence
- The cutoff at low frequency show daily variations whereas the outer scale length can be considered as an atmospheric constant of the order of 3000m

Abstract

Microwave signals, for example, those from Global Navigation Satellite Systems (GNSS) and very long baseline interferometry, are affected by tropospheric turbulence in such a way that the random fluctuations of the atmospheric index of refraction correlate the phase measurements. These atmospheric correlations are an important error source in space geodetic techniques. For computational reasons, they are neglected in positioning applications, to the detriment of a trustworthy description of the precision, and rigorous test statistics. Fortunately, modelling such correlations is possible by combining concepts from electromagnetic wave propagation in a random medium and the Kolmogorov turbulence theory. In this contribution, we will process single differences GNSS phase observations from a 300 m baseline between two different receivers linked to a common clock. After a preprocessing to filter additional error contributions, such as multipath, we will study the power spectral density of the phase residuals. We will estimate its low and high cutoff frequencies with an adapted unbiased Whittle maximum likelihood estimator. These cutoff frequencies – as predicted by turbulence theory – are related directly to the scale lengths of turbulence, i.e. the size of the eddies that correlate the GNSS observations. The study of their dependencies with the satellite geometry, day of the year, or time of the day provides new insights into the two- and three-dimensional atmospheric turbulence in the atmosphere. In addition, it contributes to improving the stochastic description of random effects impacting GNSS phase observations.

Plain Language Summary

A global navigation satellite system (GNSS) describes any satellite constellation that provides positioning on the Earth; it is part of our daily life, with applications such as telecommunications, land surveying, safety, or precision agriculture. Similar to airplanes that drop altitude suddenly, GNSS signals are affected by atmospheric turbulence: swirling motions, which we can imagine as small energy balls of a few mm diameter up to large horizontally elongated structures, will correlate the GNSS signals as they travel through the low atmosphere. Correlations can be understood as "measurements having something in common", and are an important source of errors: they lead to a lower positioning precision. The correlations due to random variations of the refractivity index created by atmospheric turbulence can be modelled from physical considerations. This allows the exciting study of atmospheric turbulence parameters after appropriate processing of the GNSS observations: (i) without expensive instruments and (ii) by simply using by-products from the positioning. The horizontal length of the swirling motions correlating GNSS observations can be estimated together with the size of the small energy structure, which shows typical day/night variations. This study provides new insights into the atmospheric turbulence, paving the way for innovative applications for the GNSS.

1 Introduction

Atmospheric turbulence created by the vertical shear of horizontal wind among others, affects the propagation of optical and microwave signals as they travel through the atmosphere (Ishimaru, 1994; Roddier, 1981; Stull, 2009; Wheelon, 2001; Pani et al. 2011). Turbulence, from mostly isotropic in the low boundary layer, becomes anisotropic -sometimes called two-dimensional (2D)- in the free atmosphere, beyond the tropospheric height of approximately 1 000 m above the ground (Gage, 1979; Kraichnan, 1974). Eddies or swirling motions act as correlating GNSS phase measurements making atmospheric turbulence an important error source for GNSS positioning with phase observations (Kermarrec & Schön, 2014; Wheelon, 2001). Whereas intensity fluctuations cause intermittent signal fading, phase fluctuations yield variations in the time of flight (Kermarrec & Schön, 2014; Kleijer et al., 2004; Nilsson et al., 2009; Schön & Brunner, 2008a).

The residuals of GNSS positioning with phase measurements provide a promising way to estimate turbulence parameters without complicated equipment (see first investigations using the structure function from Naudet 2016 or Vennebush et al., 2020). Physical considerations from electromagnetic wave propagation and concepts from the Kolmogorov turbulence theory yield a solid foundation to the description of their frequency content using power law functions (Agnew, 1992; Kolmogorov, 1941). Four slopes characterize the corresponding power spectral density (psd) over specific frequency bands (Wheelon, 2001):

- a two-slope noise coming from a Matérn process with a smoothness of -4/3 that saturates at low frequency (0-slope; Lilly et al., 2017);
- a -2/3 additional noise in the middle frequency band of the spectrum coming from a superimposed sinus term; and

- an additional white noise (WN) at very high frequencies (0-slope), which arises from aliasing and electronic components.

Two cutoff frequencies divide the spectrum and are related to the description mentioned previously. They describe the physical scales of the positioning problem under consideration:

1. the high frequency cutoff (transition smoothness -4/3 and -2/3 noise) can be thought of as being related to smaller eddies, i.e. the inner scale length of turbulence, whereas
2. the low frequency cutoff (transition -2/3 noise and saturation slope) should be an atmospheric constant, depending eventually on low periodic and large-scale atmospheric conditions, such as weather fronts (Shepherd, 1987).

The study of these two cutoffs from the residuals of GNSS positioning with phase observations provide, thus, a new insight into atmospheric turbulence and, more particularly, into the dependencies of the scale lengths of atmospheric turbulence. They will be the focus of the present contribution.

Prior to such analysis, additional effects affecting the residuals should be mitigated, such as multipath or receiver clock errors: they may bias the estimation of atmospheric parameters. In this contribution, we will make use of between-stations single differences (SDs) global positioning system (GPS) phase observations. The receiver clock fluctuations can be removed and effects of interest separated, taking benefits from a common clock assembly between receivers (Leute et al., 2016; Santerre & Beutler, 1993). This allows both a validation of the presence of the atmospheric turbulence in the residuals using different receivers and a study of temporal and spatial dependencies of the cutoff frequencies, i.e. the scale lengths of turbulence.

Cutoff frequencies are usually estimated empirically by visually identifying the point where the psd kicks off (see, e.g. Accardo et al., 1997, for an example of electroencephalographic time series for filtering the WN component. Most of the literature is related to filter design, for which the cutoff frequency refers to the frequency between, above or below which the frequencies of a signal will be blocked or attenuated (Hunter, 2001). In this contribution, we prefer an automatized and statistically-based method to an empirical visual identification of the cutoff frequency as it allows one to combine multiple time series of observations per day of the year (DOY) efficiently from more than 32 GPS satellites. Correspondingly, our analysis is built on the methodology developed in Kermarrec and Schön (2020), and adapted to the specificity of SD observations. It is based on the empirical mode decomposition (EMD) of power law noises (Flandrin et al., 2004, 2005; Wu & Huang, 2004) which permits to filter both the WN component and additional effects coming from the multipath. The cutoffs are further estimated using the unbiased WMLE, as proposed in Sykulski et al. (2019). Our strategy will be validated with Monte Carlo simulations and applied to

real SD observations for an analysis of the spatial or temporal dependencies of the cutoffs frequencies.

The remainder of the contribution is as follows: in a first section, we review the theoretical background for the expected microwave phase noise psd and how to estimate the parameters by maximum likelihood. The second section explains the processing of GPS observations using SD. We follow by presenting the results of the real data analysis focusing on the dependencies of the cutoff frequencies with time and geometry.

2 Theoretical Background

In this section, we briefly review the derivation of the psd for phase difference for atmospheric microwave transmission following Wheelon (2001, chapter 6).

1. Concept of turbulence theory

   (a) *The concept of eddies and refractivity spectra*

Any turbulent flow can be interpreted as a population of many swirling motions called eddies, vortices or swirling motions. They coexist in different sizes and strengths, embedded in one another and forever changing, giving the flow its randomness. According to Kolmogorov (1941), the energy is supplied at a macroscale and is dissipated at microscale by viscosity. The interaction among the eddies of various scales passes energy sequentially from the larger eddies to the smaller ones. This process is known as the *turbulent energy cascade* and describes the three-dimensional (3D) turbulence well. For 2D turbulence, an inverse cascade was postulated (Kraichnan, 1974), and its study remains an active research field, particularly in the atmosphere (see e.g. Hyde et al., 2015, for optical signals).

Regarding the Kolmogorov theory, we assume that the characteristics of the turbulent eddies depend solely on themselves and on the energy cascade rate. This is similar to saying that the eddies "know" their size, at which rate energy is supplied to them and at which rate they must supply it to the next smaller eddies in the cascade. The *macroscale* is typically related to the scale of the problem under consideration; this is probably the size of eddies present around the tropospheric height of approximately 1000 m for GNSS phase observations: The strength of the turbulence is still strong enough to affect GNSS phase observations, so that horizontally elongated and anisotropic eddies will act as correlating the measurements.

It is customary in turbulence theory to consider the power spectrum, i.e. the distribution of kinetic energy per mass across the various length scales. A $-5/3$ power law of the energy spectrum derived from dimensional analysis has been observed to hold true in the inertial range and beyond. Over this inertial region, Tatarski (1971) gave the Kolmogorov wave number spectrum of spatial refractivity fluctuations as

, (1)

where is the structure constant of the atmosphere, which varies with height but is considered here as a constant or global parameter for the sake of simplification of the integrations, and is the wave number or spatial frequency. This model is valid in the inertial range for homogeneous and isotropic turbulence, with being the outer and inner scale length of turbulence that bounds the inertial range, respectively.

The von Kalman spectrum is mathematically convenient as it saturates at wave number in the inertial region. It is expressed as

. (2)

We will make use of this spectrum, following Wheelon (2001); extensions all maintain the scaling , on which our investigations for the variations of the scale lengths are based.

1. *Power spectral density of phase difference*

A usual way to derive the psd of phase difference is to assume the medium to be frozen, moving with a constant wind speed , perpendicular to the signal propagation. This assumption is justified at the tropospheric height for GNSS signals: at that height, the horizontal geostropic wind blows with a constant velocity of approximately 8 ms^{-1}. This so-called Taylor hypothesis (Taylor, 1938) allows one to express spatiotemporal quantities as being only temporal. This makes some integrations manageable, so that an expression for the phase difference of microwaves propagating through the atmosphere can be derived. The van Karman spectrum leads to a phase difference psd with three dominant power law processes which we summarize as:

, (3)

where is an angular cutoff frequency proportional to the wind velocity. Accompanying this contribution, we will allow ourselves to write loosely "-8/3" or "-2/3" noise, depending on the slope of the psd from Eq. (3).

Regarding the station separation perpendicular to the GNSS signal propagation plane and a wind vector parallel to the station separation, we have:

, (4)

where is the phase psd expressed as

(5)

with , the elevation angle of the satellite.

One can conjecture that the slopes of the psd will not be affected if the wind is not blowing perpendicularly to the baseline (Wheelon, 2001, problem 7). If the wind direction at the tropospheric height does not change strongly during the experiment, no influence on the dependencies of the cutoff frequencies is expected, or, at least, no influence within the confidence level for determining the parameter.

The previous description is based on further assumptions, such as the Taylor frozen hypothesis of the medium (Taylor, 1948), the constant velocity of the wind, and a height independent structure constant, which measures turbulence strength (Nilsson & Haas, 2010). Wheelon (2001, chapter 6.5.5.4) discusses the doubtfulness of these approximations for long baselines. This is unproblematic here as we will use SD from a short baseline.

The reader is referred to Appendix 1 for a better understanding of the cutoff frequencies; it explains graphically and intuitively the difference between and .

1. *Cutoff frequencies*

In this section, we propose to summarize the physical interpretation of the cutoff frequencies of Eq. (3) and a method to estimate them with high trustworthiness, throwing light on the related challenges and inherent limitations of the estimation method.

1. *Physical interpretation of the cutoff frequencies*

- Following Wheelon (2001, chapter 6), is the outer scale of turbulence of microwave measurements and is related to the horizontal elongation of the anisotropic eddies present at the tropospheric height. It was found in previous studies to be around 3000 m (Kermarrec, 2020; Kermarrec & Schön, 2014), assuming a constant geostropic wind velocity of 8 ms^{-1}.
- The understanding of is slightly more challenging. In an interferometric application with phase differences, is proportional to the distance between two antennas on the ground (Wheelon, 2001). Dealing with GNSS SD, we propose to interpret this cutoff as being related to an inner scale length and homogeneous with an angular frequency. Correspondingly, determines the transition between the 3D turbulent regime (-8/3 slope) and the anisotropic regime (-2/3 slope). Variations of will be related to the strength of the 3D turbulence: this angular frequency will most probably have some similarities with variations of the atmospheric structure constant. Please refer to Nilsson et al. (2009) for more details on this important atmospheric parameter. Consecutively and similarly to , the quantity should depend on the wind velocity below the tropospheric height, where the isotropic turbulence dominates.
- The transition between the high and low frequency regime is to be linked with the multiple eddy sizes that affect GNSS signals through their atmospheric travel.

1. *Challenges raised by the determination of the cutoff frequencies*

The estimation of the two cutoff frequencies or scale lengths of turbulence is related to the correct identification of the three bandwidth noises. Adding a WN at high frequencies, we even face the challenge of four noise processes from which we want to estimate two scale lengths as accurately as possible. In the following, we propose to briefly illustrate the challenges linked with the

determination of the cutoff frequencies following the example taken in Appendix 1. is taken lower than in the example of Appendix 1 with the aim of modelling a stronger 3D turbulence. We note that the example of this contribution should provide the reader with an insight into the variety of psd that can be obtained by varying the turbulent parameters.

- Variation of the cutoff frequencies

Figure 1 (top left) presents the psd by taking to 0.3 and 0.4 rad/sample (blue and red line, respectively) with fixed at 0.015 rad/sample. As intuitively expected, the psd evolves to the -2/3 slope for rad/sample earlier than for . This has hardly any impact on the low frequency region and the two psd generated saturate visually at approximately rad/sample, which is close to the simulated value of 0.015 expected.

On the contrary, if we vary from 0.015 to 0.02 (blue and yellow lines, respectively), the high frequency region is not affected but the yellow psd clearly saturates before the blue one, which is expected.

- The presence of WN

A challenge for the estimation of

In order to mimic a real scenario, we modelled the spectral density by , with , the psd of WN, coming from the processing of the observations from the GNSS receiver, aliasing and quantization effects. Figure 1 (top right) shows that the WN component affects the determination of , whereas the low frequency part of the psd remains unchanged. The shorter the bandwidth of the -8/3 noise, the more challenging the determination of . We notice that without WN (red line), the sinus term of Eq. (5) affects the high frequency part strongly; the visual identification of is hardly possible: fortunately, this is an improbable scenario in a real case.

A bias toward 0: a need for whitening

Visually, is shifted towards high frequencies due to the presence of WN (blue line in Fig. 1, bottom left): the -8/3 slope cannot be clearly identified and is underestimated. We performed a WN filtering using the methodology presented in Section 2.2.3 and were able to correct the overestimation of and the slope of the psd (red line). This result is an indication that the WN component should be filtered out prior to estimating the cutoff at high frequency. Exemplarily, if we increase the WN from 0.1 to 0.5 db/Hz (Fig. 1, top right, yellow line), the -8/3 noise may even disappear, so that the transition goes directly from WN to -2/3 noise.

- A parallel between slope and cutoff frequency variations.

Some previous contributions using Zenith Total Delay found some discrepancies with the Kolmogorov theory from, for example, the slope of the structure function (Kube & Schön, 2015; Nilsson et al., 2009). The previous example may

have given the reader some insight about the challenges linked to the risky underestimation of power law slopes and overestimation of the cutoff frequencies in the presence of additional WN at high frequency. Similarly, non-modelled low frequency noise can lead to a biased . It may even be impossible to estimate this value if the psd does not saturate because of, for example, flicker noise (Ward & Greenwood, 2007).

We are strong believers that discrepancies from the Kolmogorov theory are more likely to be linked to the presence of additional and non-filtered noise that makes the estimation of psd slopes challenging; Previous studies showed a more probably biased estimation of the parameters under consideration as no filtering was performed. In this contribution, we, thus, do not wish to doubt the validity of the Kolmogorov theory but stay aware of the limitation related to the cutoff/slopes estimations.

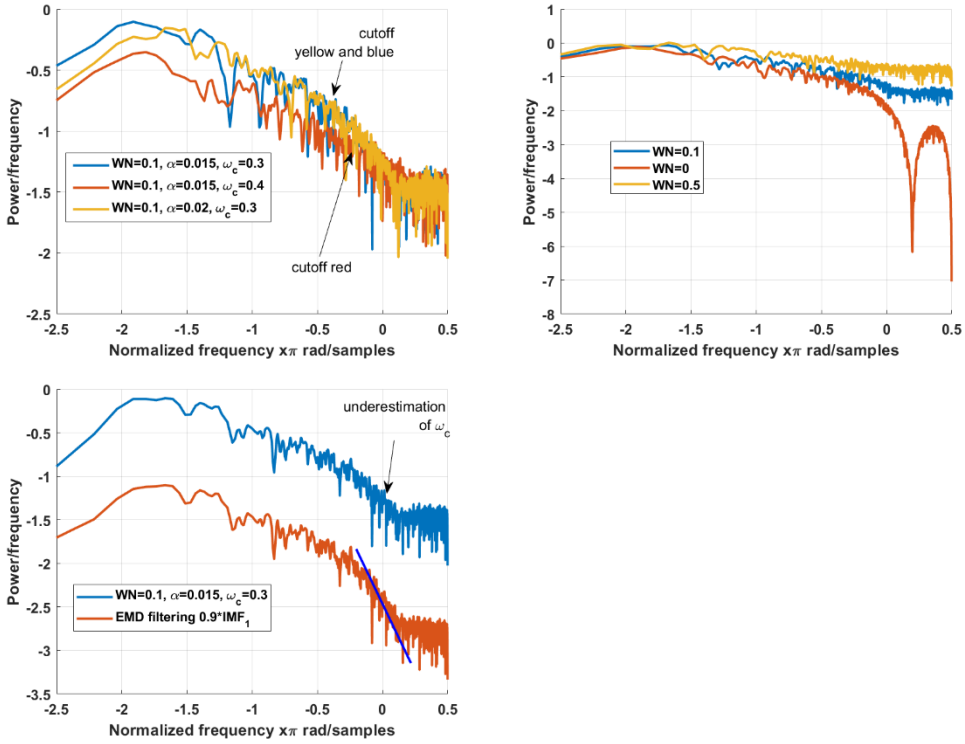

Fig. 1: Top left: psd in db/Hz of simulated time series by varying the cutoff frequencies and Top right by varying the WN component. Bottom left: the impact of WN on the identification of and the -8/3 slope. All psd are in a loglog plot.

We propose estimating the cutoffs based on statistical methods rather than visual identification for increased trustworthiness. We summarize the related

challenges as follows:

- filter the WN component at high frequencies to avoid an overestimation of the cutoff due to both a short bandwidth and a biased slope of the turbulent noise;
- find an estimator for the cutoff at low frequency. This necessitates filtering low frequency noises, such as random walk or flicker noise, which may mask the transition between regimes.

In the next section, we present the methods chosen for the noise mitigation and parameter estimation.

1. *Noise mitigation*

The proposal for determining the cutoff frequencies follows Kermarrec & Schön (2020) and makes use of the EMD and its extension, the Hilbert Huang Transform (Wu, 2009; Wu & Huang, 2004) to reduce the multipath effect and filter high frequency noise. The EMD is an empirical method and suits the analysis of GNSS residuals best. Its main derivations are given in Appendix 3 with the aim of not affecting the reading flow and are here only briefly summarized in a flowchart form in Figure 2.

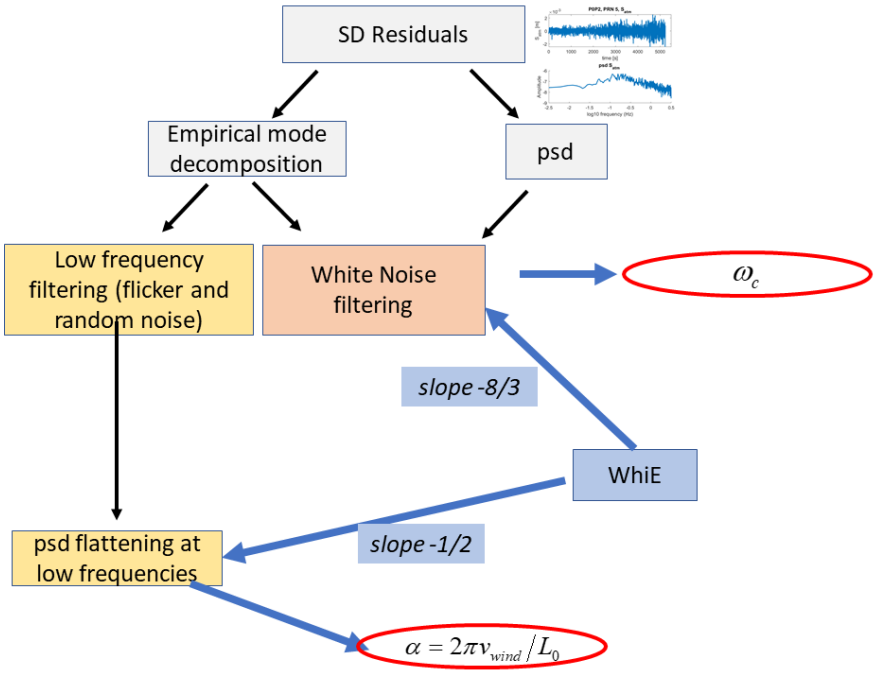

Fig. 2: Explanation of the methodology to filter and estimate the cutoff frequencies

Elimination of low frequency noise

The basic idea to mitigate the effect of additional low frequency noise is based on the elimination of so-called intrinsic mode functions (IMFs) from the EMD. Consequently, we make use of the property that the log2 variances of the IMF versus the level of decomposition follow a straight line with a given slope depending on the power law of the noise psd. Additional effects translate into stronger power at a low frequency, up to an additional random walk (see e.g. He et al., 2019). If a slope corresponding to another power law noise is detected for a higher IMF, a filtering is mandatory, as explained in Appendix 2.

Elimination of WN

The elimination of the WN is mandatory to avoid a biased estimation of the cutoff . We use the expectation–maximization algorithm developed in Kargoll et al. (2018). The latter is best suited in the presence of outliers, which are inevitable in a real case. We determine the ratio between WN and power law noise to downweigh the first IMF of the EMD.

1. *Estimation of cutoff frequencies*

Once the residuals have been preprocessed, the cutoff can be estimated by means of an unbiased version of the Whittle Maximum likelihood (Sykulski et al., 2019). This procedure was shown to be trustworthy, even for small sample sizes. Accordingly, we use the Matlab function maternfit from Lilly (2020). This function allows one to fix the slope to a given value so that *only* the cutoff parameter has to be estimated. The latter can be further forced within a given interval. In our case, this is strongly advantageous as physically based estimations of the parameters are available: assuming m and a wind velocity of 8 ms^{-1}, we can estimate rad/sample (see Appendix 2). Similarly, physical considerations provide values between 0.8 and 1.2 rad/samples for following Kermarrec and Schön (2020).

Correspondingly:

- for the estimation of , we fix the slope in the estimator to -8/3, as we do not question the theoretical finding. The psd does not saturate at but changes its slope: we need to specify the interval within which has to be searched to avoid its biased estimation.
- We search for the saturation frequency of the Matérn model for the estimation of . Unfortunately, the Matérn model is not defined for slopes smaller than -1/2 (Guttorp & Gneiting, 2005). We expect to find a slight underestimation of the parameter due to the discrepancy with the -2/3 slope. Monte Carlo simulations are, thus, necessary to quantify this effect and validate the methodology.
- The batches of observations should be long enough to allow for saturation to estimate the outer scale length of turbulence. Assuming rad/sample, the batch length – or number of observations – should be at least 2000 for 1 Hz observations (Sykulski et al., 2019).

1. *Validation of the methodology using Monte Carlo simulation*

In order to validate our methodology for estimating the cutoff frequencies with the unbiased WMLE, we generated 1000 noise samples each of a length of 5000 from the psd derived in Eq. (4). The same values as previously were taken, i.e. a WN component of 0.1 db/Hz and rad/sample.

- Firstly, we performed a WN whitening and found a mean coefficient of 0.09 +/-0.003 to be applied to the first IMF.
- Using our methodology based on the log2 variances of the EMD, the low frequency cutoff was found to be a mean of 0.0153 +/-1e^{-4}, which corresponds to a discrepancy for the outer scale length of approximately 100 m. Regarding that, (i) this value is unknown in a real case, (ii) we make use of the estimator by specifying a higher power law than expected in the simulated time series and allows ourselves to be satisfied with this (small) bias. Variations are important for our investigations: a coherency in the estimation and the filtering strategy is mandatory rather than trying to access the unknown true value of this parameter.
- The high frequency cutoff could be estimated as a mean of 1.02 +/-2e^{-3} rad/sample.

We find the results of the Monte Carlo simulations acceptable, bearing in mind that no reference is available for comparison when dealing with real data. In the next section, we propose applying this methodology to SD from GPS observations with the aim of studying the variations of the cutoff frequencies but *not* searching for their exact value.

1. **Real Data Analysis**

3.1. Experimental setup

In October 2013, we conducted a measurement campaign at the Physikalisch Technische Bundesanstalt (PTB), Germany's national metrology institute in Braunschweig. The setup was operated in the context of the research project "Surveying" funded by the European Metrology Research Program (Pollinger et al., 2015). Various receiver antenna combinations were operated at the Meitner and Kopfermann building over three weeks. The data analyzed in this paper includes DOY 297 (October 24, 2013) and DOY 298 from the stations KOP1 and MEI1 (cf. Fig. 3). The station at the Meitner building is free of obstructions because it is located above the trees at the PTB campus, while KOP1 shows partial signal obstruction up to elevations of 25°. The baseline between the two stations has a distance of 290 m and a height difference of 16 m.

Both stations were equipped with a Leica AR3 choke ring antenna with radom LEIT, each of which is individually and absolutely calibrated at IfE Hannover (Kröger et al., 2021). A JAVAD Delta and a Leica GRX1200 receiver were connected to each antenna via an active signal splitter, respectively. All receivers were fed with a common H-maser quality ("UTC-PTB") frequency input via

fiber links (cf. Leute at al., 2016, for the details of the installation and operation of the fiber link). The data rate was 1 Hz and the cutoff angle 0 degrees. The data quality is shown in the sky plots of both stations containing the color-coded C/N0 values (Fig. 4). The comparison shows the reduced signal strength (blue colors) at low elevation angles for the Kopfermann building, induced by the signal diffraction and partial obstructions by trees and foliage. The reference coordinates have been precisely determined by long-term measurements for MEI1 and are known from PTB in the case of the antenna post KOP1.

Fig. 3: Experimental setup at the PTB Campus Braunschweig, Germany. Top: google view of the scene showing the GNSS stations PTBB and KOP1 at the Kopfermann building (left) and the stations MEI1 and MEI2 at the Meitner building located about 290 m west and above the trees. Bottom zoom on the antennae installed at KOP1 and MEI2 used in this study.

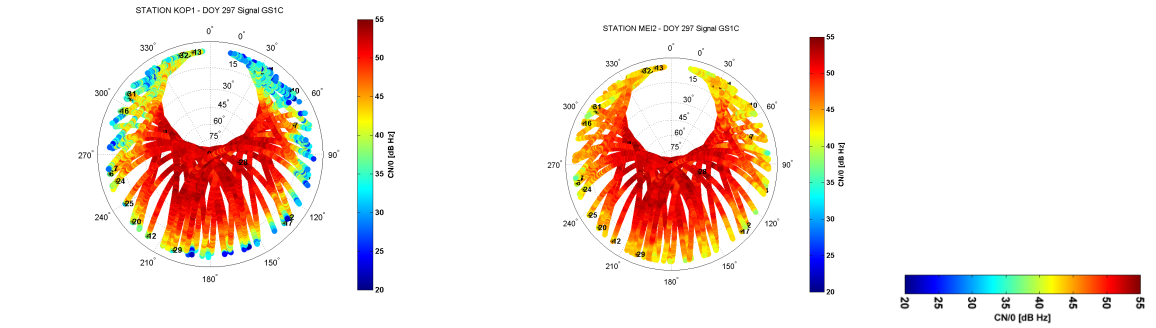

Fig. 4: Satellite sky distribution at the two stations used in this study (KOP1, left, MEI2 right) color coded by the carrier to noise ratio indicating the signal quality for DOY 297

1. Data processing

In the following, we will analyze the carrier phase signals. The observation equation for a carrier phase measurement between a satellite k and a user A can be modelled by

, (6)

where denotes the Euclidian distance between the unknown user position and the computed satellite position at the time of signal transmission, the synchronization error between the satellite and receiver clock, and the tropospheric delay and ionospheric signal advance, respectively. Further corrections must be applied, for example, to antenna phase center corrections and phase wind up. The wavelength of the signal is denoted by , the ambiguity is , the multipath effect is described by and the observation noise of typical 1–2 mm by . Interested readers can refer to the basics of GNSS positioning in the textbooks (e.g. Leick et al., 2015).

The common clock setup allows one to form between-receiver SDs on the 280 m baseline MEI1 – KOP1 for common or mixed receiver pairs and at the zero baseline at the two stations with mixed receiver types. This setup eliminates the satellite clock and orbit errors and greatly reduces the ionospheric effects. The cutoff angle for the analysis was set at 15° to take the challenging conditions at KOP1 into account. The minus-computed observations of the SD time series contains a constant combined clock and ambiguity offset, atmospheric noise, receiver noise, multipath effects, and noise from asymmetries in the setup. Figure 5 presents the corresponding setup in a condensed form.

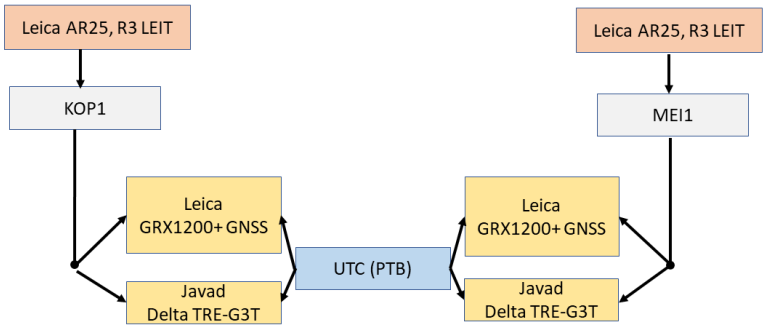

Fig. 5: Setup for the experiment performed with a common clock, SD processing

3.3. Analysis of the SD and determination of the cutoff frequencies

3.3.1. Cutoff frequencies

We wish to estimate both and (and per extension) from the real GPS observations as developed in Section 2.

Our data set is unique and allows us to answer:

1. whether the receiver has an impact on the cutoff frequencies,
2. whether the DOY and/or the time of the day influences the parameters, and
3. if the cutoff frequencies depend on the satellite geometry. As geometry, we understand the elevation and azimuth of the satellites.

The following results can be expected:

- is related to the outer scale length of turbulence . This parameter is more likely to be an atmospheric constant depending on the scale of the problem (Busher et al. 1995, Wheelon, 2001, Wheelon et al. 2005, McCrae et al. 2019). The meteorological conditions were stable during the experiments described in this contribution, so that variations from day to day due to, for example, fronts, are not expected. Variations of for a longer time span remain the topic of a dedicated study.
- should be related to the strength of the isotropic turbulence. We expect a variation between (i) night, during which stable conditions should lead to bigger eddies, and (ii) day, with a mixed and quickly reorganizing medium. The topology of the experiment combined with the stable meteorological

condition makes us optimistic about finding this dependency. The path of the GPS rays through the atmosphere is longer for a low elevation leading to a stronger impact of the 2D turbulence: a higher for batches with low elevation observations can be expected.

The intuitive expectations necessitate an orientation of the processing of the residuals as follows:

- An accurate determination of necessitates that enough observations are available (at least 2000): we will estimate this parameter from one entire batch of observations, preprocessed following the methodology developed in Section 2. Consecutively, the elevation dependency of is more difficult to assess as the elevation is averaged over one batch. We know from the Monte Carlo simulation that we can expect an accuracy of 100 m at best.
- Regarding studying and its time variability, we need to cut the batch of observations of one satellite arc into smaller ones; a higher number of values will be obtained, which allows us to study the parameter variations during the day. We consider that at least 2000 observations are necessary to determine using the Whittle maximum likelihood, consequently, the batches were selected with a 15° elevation step. Batches with fewer than 2000 observations were eliminated. Unfortunately, we could not find satellites present at the same time and perpendicular rays to investigate the variations of regarding the orientation with the wind vector (Wheelon, 2001, p. 310).

The methodology used in the real data analysis is summarized in Fig. 6. Please note that a preprocessing following the methodology of Section 2 is applied to mitigate the combined effects of the remaining multipath and WN and avoid biased estimates of the cutoff frequencies.

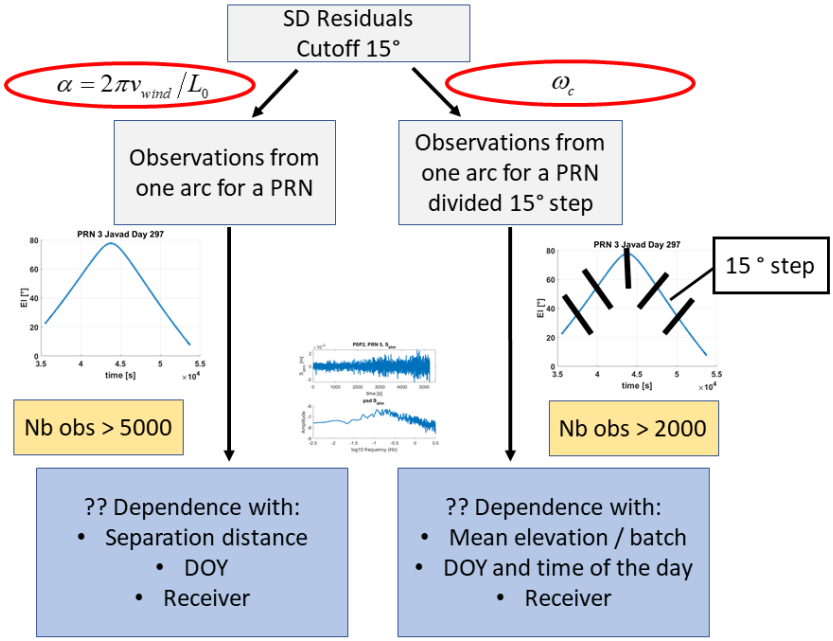

Fig. 6: Methodology and intuitive expectation for the real data analysis for the low and high cutoff frequencies

3.3.2. Results and comments

Low frequency cutoff

We firstly investigate the dependencies of the low frequency cutoff . The numerical results for the mean of regarding all batches for the two DOYs under consideration are presented in Table 1 together with their standard deviations. We computed the cutoff for each arc of observations from each satellite above the elevation cutoff of 15°. No whitening was performed as the latter does not affect the low frequency domain regarding the expected value of 3000 m.

We plotted for the two receivers and the two DOYs in Figure 7 against

- the maximum of the separation distance for each arc of observations (one batch) computed as the distance between two GPS rays at the tropospheric height (Kermarrec & Schön, 2020),
- the mean epoch of the batch expressed in hours, and
- the mean azimuth and the elevation for one batch of observations.

The blue and red stars correspond to Javad and Leica, respectively.

The conjecture from Table 1 that should be close to an atmospheric constant is confirmed: the values found for both receivers and DOYs are close and coherent

with values found for the cutoff obtained with double differences phase observations. The value is independent of the processing of the phase observations (Kermarrec & Schön, 2020). The standard deviation is around 400 m, which remains an acceptable value provided that , interpreted as the size of horizontally elongated eddies, has no "accuracy." Figure 7 (bottom left) further highlights that is nearly constant during the whole day. Similarly, no dependencies with the elevation or azimuth are found and is also not linked with the separation distance between two GPS rays but is rather a physical quantity specific to GPS microwave signals. The extent to which this value applies to GLONASS, Beidou or Galileo satellites remains the topic of a dedicated contribution.

Tab. 1. Results for and in [m] and [rad], respectively, for the two DOYs and receivers under consideration. The whole arc of observations for one satellite was used for the computation. We provide the mean value over all batches. The standard deviation is given in italics.

DOY 297	[m]	DOY 298	[m]
Javad	3792 *(410)*		3790 *(400)*
Leica	3835 *(410)*		3800 *(420)*
DOY 297	[rad]	DOY 298	[rad]
Javad	0.15 *(0.06)*		0.16 *(0.05)*
Leica	0.23 *(0.05)*		0.24 *(0.05)*

High frequency cutoff

The spatial high frequency cutoff was computed batch-wise by 15° elevation steps to provide a better analysis of its dependencies. The following remark based on Figure 8 is worth making:

- the values for the two receivers are not similar: values obtained from the Leica GRX1200 receiver are shifted by approximately +8 rad compared to the one from the Javad receiver. This difference may be due to the internal noise processing at the receiver level. We computed the factor needed to downweigh the first IMF and found a mean value of 0.47 (std 0.03) for both the DOY with the Javad receiver and 0.55 (std 0.04) for the Leica receiver. The WN component is, thus, receiver-dependent and slightly stronger for the Leica receiver. This may cause the discrepancy. We are interested in variations of the parameters. Consecutively, we point out that the processing should be obligatory performed similarly for all batches for the sake of comparison.

Figure 8 gives a new insight into the dependencies of regarding the satellite geometry or the time of the day. The main results can be summarized as follows:

- The behaviour of for the two different DOYs is comparable to the two receivers, which we link with the repeating satellite constellation from day

to day.

- A clear periodic variation with the time of day is visible for both receivers: is large around 10 h, decreases until 18 h, increases at the beginning of the night and decreases to reach a minimum around 2 h at night. This corresponds to a more stable atmospheric condition and a decrease of turbulence. This specific periodic shape is similar for the daily variations of the atmospheric structure constant for optical signals, as shown exemplarily in Weiss-Wrana and Salem Balfour (2002) or Shao et al. (2016). This result confirms that is related to the strength of the isotropic turbulence. This effect is slightly less visible for the Leica receiver on DOY 297, although damped due to the lower strength of the noise for this receiver. We note a shift of approximately half an hour in the maximum around 10 h for the two receivers, which we propose not to overinterpret due to the challenge related to the estimation of .
- There is no dependency of regarding the azimuth.
- A dependency with the mean elevation of the satellite per batch can be identified from Figure 8. is higher for low elevation satellites (15–20°), decreases significantly by nearly a factor of 2 for both receivers and increases for high elevation satellites (70–80°). This finding seems logical: as the elevation decreases, the GPS signals will be more affected by 2D turbulence and increases. This finding has probably a slightly different interpretation for high elevation satellites and may be related to the mean inner scale length of the travelled medium "viewed". The latter decreases due to the higher sensing rate of the atmosphere by the GPS signals at a high elevation. We note that the shape differs slightly for the two receivers, due most probably to the internal processing mentioned previously.

a) DOY 297 b) DOY 298

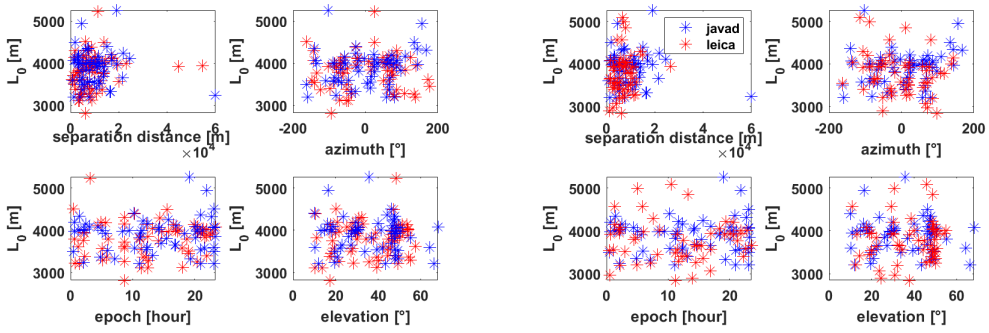

Fig. 7: a) Javad (red) and Leica (blue) receiver DOY297: left top: versus separation distance [m], right top: versus azimuth [°], left bottom: versus time

of the day [hour], right bottom: versus elevation in [°]. b) same DOY298

a) DOY 297 Javad receiver

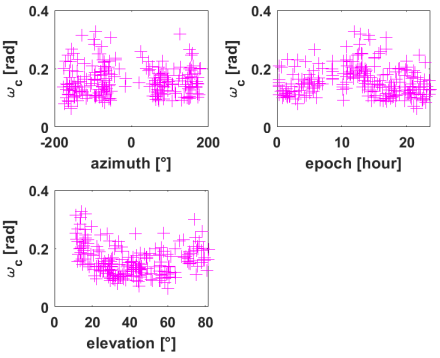

b) DOY 298 Javad receiver

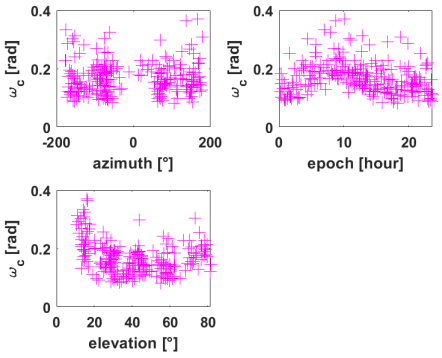

c) DOY 297 Leica receiver

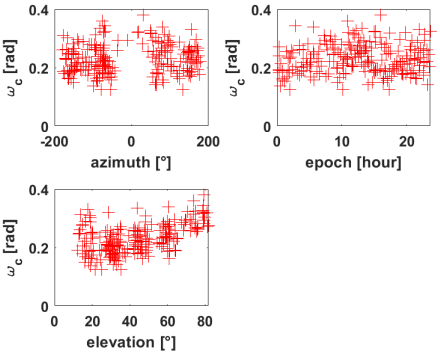

d) DOY 298 Leica receiver

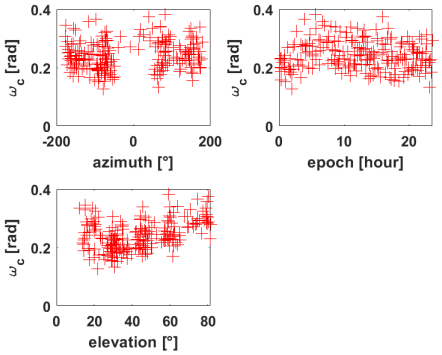

Fig.8 a) Javad receiver DOY297: left top: versus azimuth [°], right top: versus time of the day [hour], left bottom: versus elevation in [°].

b) Javad receiver DOY298, c) Leica receiver DOY297, d) Leica receiver DOY298

1. **Conclusion**

Provided that the clock error has been retrieved, the SD time series of minus-computed GNSS carrier phase observations provide a unique way of studying the turbulent or atmospheric noise. The psd of the noise due to atmospheric turbulence for microwave phase difference measurements can be derived from physical considerations and using (i) the Kolmogorov theory and (ii) the Taylor frozen hypothesis. It has four slopes corresponding to different regimes of turbulence and observation noise. The corresponding cutoff frequencies of this bandwidth noise can be associated with the size of the eddies that affects GNSS measurements: at low frequency, horizontally elongated eddies are stable and

linked with 2D turbulence or large-scale atmospheric effects. On the contrary, smaller isotropic eddies reorganize themselves quickly and are associated with the 3D turbulence. They correspond to the high frequency cutoff.

The challenge beyond the study of the turbulent noise from GNSS residuals lies in estimating these frequencies with a high trustworthiness to allow for a physical interpretation of their dependencies. In this contribution, we proposed using the EMD to filter additional unwanted effects, such as multipath or WN. The WMLE chosen was shown to perform adequately for retrieving the cutoff frequencies by means of Monte Carlo simulations.

The filtering and estimation method were used in a real case with the SD from two pairs of different types of GNSS receivers linked by a common clock. The observations were affected only a little by the multipath. The meteorological conditions were stable for the two DOYs under consideration. We found that the outer scale length of turbulence was nearly the same for both receivers and days; this is coherent with the interpretation of this value as an atmospheric constant and is expected from the van Karman spectrum of turbulence. On the contrary, variations with the time of the day could be found for the high frequency cutoff, probably linked with more stable atmospheric conditions at night and daily variations of the wind and, thus, turbulence strength. A dependency on the elevation could be found, which seemed coherent with the longer propagation path through and the sensing of the atmosphere.

Our investigations validated that SD observed minus-computed observations with a common clock have a great potential in giving new insights into the turbulent structures affecting the GPS microwave propagation. The results supported our intuitive expectations. Additional work has to be done to extract the bandwidth noise more accurately and estimate its strength to derive further atmospheric parameters, such as the structure constant or variations of the wind velocity. Further analysis should be performed to confirm the dependencies using observations with different antennae. This study supports the setting of nonempirical, fully populated variance-covariance matrices in a positioning adjustment for a more realistic precision.

Funding

This study is supported by the Deutsche Forschungsgemeinschaft under the project KE2453/2-1, as a pre-step to the analysis of atmospheric noise from a terrestrial laser scanner. The data from the GPS experiment was captured within the research project “Surveying” funded by the European Metrology Research Program.

Authors’ contributions

GK developed the methodology to extract and interpret the bandwidth atmospheric noise based on EMD decomposition and made the analysis of the SD residuals. She wrote the manuscript. SS and TK discussed the results and contributed to the part on GPS processing and the dataset description.

Acknowledgements

Le Ren is warmly thanked for having processed the SD analyzed in this contribution. Dr. Thomas Krawinkel set up the GNSS measurements. We further thank Dr. Andreas Bauch und Julia Leute, both from PTB, for operating the common clock experiment.

Data Avaibility Statement

Data archiving in underway. We will use the repository of the Leibniz University Hannover. Until the archiving is achieved, the data are uploaded as supporting information.

References

Accardo, A., Affinito, M., Carrozzi, M.. & Bouquet, F. (1997). Use of the fractal dimension for the analysis of electroencephalographic time series. *Biological Cybernetics, 77*, 339–350.

Agnew, D. C. (1992). The time-domain behaviour of power-law noises. *Geophysical Research Letters*, *19*(4), 333–336.

Brockwell P.J. and Davis, R.A. (1991). Time Series: Theory and Methods. 2nd Edition, Springer-Verlag, New York. doi:10.1007/978-1-4419-0320-4

Buscher, D. F., Armstrong, J. T., Hummel, C. A., Quirrenbach, A., Mozurkewich, D., Johnston, K. J., et al. (1995). Interferometric seeing measurements on Mt. Wilson: Power spectra and outer scales. *Applied Optics*, *34*, 1081–1096.

Flandrin, P., Gonçalvès, P., & Rilling, G. (2005). EMD equivalent filter banks, from interpretation to applications. In N. E. Huang, S. S. P. Shen (Eds.), *Hilbert-Huang transform and its applications* (Vol. 5, pp. 57–74). Singapore: World Scientific.

Flandrin, P., Rilling, G., & Gonçalvès, P. (2004). Empirical mode decomposition as a filter bank. *IEEE Signal Processing Letters*, *11*, 112–114.

Gage, K. S. (1979). Evidence for a k to the -5/3 law inertial range in mesoscale two-dimensional turbulence. *Journal of the Atmospheric Sciences*, *36*, 1950–1954.

Guttorp, P., & Gneiting, T. (2005). *On the Whittle-Mátern correlation family.* NRCSE Technical Report Series n°80.

He, X., Bos, M. S., Montillet, J. P., & Fernandes, R. M. S. (2019). Investigation of the noise properties at low frequency in long GNSS time series. *Journal of Geodesy*, *93*, 1271–1282. DOI: 10.1007/s00190-019-01244-y

Huang, N. E., & Shen, S. S. P. (2005). *Hilbert-Huang transform and its applications. Interdisciplinary mathematical sciences* (Vol. 5). New Jersey: World Scientific.

Hunter, I. C. (2001). *Theory and design of microwave filters*. The Institution of Engineering and Technology.

Hyde, M. W., Basu, S., & Schmidt, J. D. (2015). Two-dimensional simulation of optical wave propagation through atmospheric turbulence. *Optical Letters*, *40*, 233–236.

Ishimaru, A. (1997). *Wave propagation and scattering in random media*. New York: IEEE Press and Oxford University Press.

Kargoll, B., Omidalizarandi, M., Loth, I. et al. (2018). An iteratively reweighted least-squares approach to adaptive robust adjustment of parameters in linear regression models with autoregressive and t-distributed deviations. *J Geod* **92,** 271–297.

Kermarrec, G. (2020). On estimating the Hurst parameter from least-squares residuals. Case study: Correlated terrestrial laser scanner range noise. *Mathematics*, (5), 674. DOI: 10.3390/math8050674.

Kermarrec, G., & Schön, S. (2014). On the Mátern covariance family: A proposal for modeling temporal correlations based on turbulence theory. *Journal of Geodesy*, *88*(11), 1061–1079. DOI: 10.1007/s00190-014-0743-7.

Kermarrec, G., & Schön, S. (2020). On the determination of the atmospheric outer scale length of turbulence using GPS phase difference observations: the Seewinkel network. *Earth, planets and space*, *72*(1), 184.

Kleijer, F., Elosegui, P., & Davis, J. L. (2004). Characterizing atmosphere turbulence with GPS. *Bulletin of the American Meteorological Society*, *85*(9), 6–15.

Kolmogorov, N. A. (1941). Dissipation of energy in the locally isotropic turbulence. *Doklady Akademii Nauk SSSR [Proceedings of the USSR Academy of Sciences]*, *32*, 16–18 (Russian).

Kraichnan, R. H. (1974). On Kolmogorov's inertial range theories. *Journal of Fluid Mechanics*, *62*(2), 305–330.

Kröger, J., Kersten, T., Breva, Y., & Schön, S. (2021). Multi-frequency multi-GNSS receiver antenna calibration at IfE: Concept – calibration results – validation. *Advances in Space Research*, January. DOI: 10.1016/j.asr.2021.01.029.

Kube, F., Schön S. (2015**).** PPP carrier phase residual stacking for turbulence investigations, 26th General Assembly of International Union of Geodesy and Geophysics (IUGG), June 22nd - July 2nd, Prague, Czech Republic.

Leick, A., Rapoport, L., & Tatarnikov, D. (2015). *GPS satellite surveying* (4th edition). Hoboken, NJ: John Wiley & Sons, Hoboken.

Leute, J., Bauch, A., Schön, S., & Krawinkel, T. (2016). *Common clock GNSS-baselines at PTB*. Proceeding of the Joint International Symposium on Deformation Monitoring 2016.

Lilly, J. M. (2020). jLab: A data analysis package for Matlab, v. 1.6.7c. http://www.jmlilly.net/jmlsoft.html.

Lilly, J. M., Sykulski, A. M., Early, J. J., & Olhede, S. C. (2017). Fractional Brownian motion, the Matérn process, and stochastic modeling of turbulent dispersion. *Nonlinear Processes Geophysics*, *24*, 481–514.

McCrae, J. E., Rice, C. A., Bose-Pillai, S. R., & Fiorino, S. T. (2019). *Investigating the outer scale of atmospheric turbulence with a Hartmann sensor*. 2019 IEEE Aerospace Conference, 2019, pp. 1–6, doi: 10.1109/AERO.2019.8741993

Michael. (2021). TimeseriesFromPSD(Sxx, fs, T, plot_on) (https://www.mathworks.com/matlabcentral/fileex timeseriesfrompsd-sxx-fs-t-plot_on), MATLAB Central File Exchange. Retrieved November 20, 2020

Montillet, J-P., Tregoning, P., McClusky, S., & Yu, K.(2013). Extracting white noise statistics in GPS coordinate time series. *IEEE Geoscience and Remote Sensing Letters*, *10*, 563–567.

Naudet, C. J. (1996). *Estimation of troposperic fluctuations using GPS data*. The Telecommunications and Data Acquisition Progress Report, TDA PR 42-126, April-June 1996, pp. 1–19.

Nilsson, T., Davis, J. L., & Hill, E. M. (2009). Using ground-based GPS to characterize atmospheric turbulence *Geophysical Research Letters*, *36*, L16807. doi:10.1029/2009GL040090.

Nilsson, T., & Haas, R. (2010). Impact of atmospheric turbulence on geodetic very long baseline interferometry. *Journal of Geophysical Research*, *115*, B03407.

Pany, A., Böhm, J., MacMillan, D., Schuh, H., Nilsson, T., & Wresnik, J. (2011). Monte Carlo simulations of the impact of troposphere, clock and measurement errors on the repeatability of VLBI positions. *Journal of Geodesy*, *85*, 39–50

Pollinger, F., Bauch, A., Meiners-Hagen, K., Astrua, M., Zucco, M., Bergstrand, S., et al. (2015). *Metrology for long distance surveying: A joint attempt to improve traceability of long distance measurements*. IAG 150 Years – Proceedings of the 2013 IAG Scientific Assembly, Potsdam, Germany, 1–6 September, 2013, International Association of Geodesy Symposia, Vol. 143, Springer International Publishing Switzerland. doi: 10.1007/1345_2015_154.

Roddier, F. (1981). The effects of atmospheric turbulence in optical astronomy. *Progress in Optics*, *19*(281), 376. doi: 10.1016/S0079-6638(08)70204-X.

Santerre, R., & Beutler, G. (1993). A proposed GPS method with multi-antennae and single receiver. *Bulletin Géodésique*, *67*, 210–223.

Shao, S. Y., Li, X. B., Li, Y. J., Zhu, W. Y., Kang, D. Y., Fan, C. Y., & Weng, N. Q. (2016). Daily variation analysis of atmospheric turbulence from inland to open sea. *Journal of Physics: Conference Series*, *679*. doi:10.1088/1742-6596/679/1/012051.

Schön, S., & Brunner, F. K. (2008a). Atmospheric turbulence theory applied to GPS carrier-phase data. *Journal of Geodesy*, *82*, 47–57.

Schön, S., & Brunner, F. K. (2008b). A proposal for modeling physical correlations of GPS phase observations. *Journal of Geodesy*, *82*(10), 601–612.

Shepherd, T. G. (1987). Inhomogeneous two-dimensional turbulence in the atmosphere. In G. Comte-Bellot, J. Mathieu (Eds.), *Advances in turbulence* (pp. 269–278). Berlin, Heidelberg: Springer. doi: 10.1007/978-3-642-83045-7_31.

Stull, R. B. (2009). *An introduction to boundary layer meteorology*. Berlin, Heidelberg: Springer Verlag.

Sykulski, A. M., Olhede, S. C., Guillaumin, A. P., Lilly, J. M., & Early, J. (2019). The debiased Whittle likelihood. *Biometrika*, *106*(2), 251–266.

Tatarskii, V. I. (1971). *Wave propagation in a turbulent medium*. New York: McGraw-Hill

Taylor, G. I. (1938). *The spectrum of turbulence*. Paper presented at Proceedings of the Royal Society London, Series A CLXIV, pp. 476–490.

Ward, L., & Greenwood, P. (2007). 1/f noise. *Scholarpedia*, *2*(12), 1537.

Weiss-Wrana, K., & Salem Balfour, L. (2002). *Statistical analysis of measurements of atmospheric turbulence in different climates*. Paper presented at the Proceedings of the SPIE 4538, Optics in Atmospheric Propagation and Adaptive Systems IV, 29 January. doi: 10.1117/12.454395.

Wheelon, A. D. (2001). *Electromagnetic scintillation*. Cambridge, New York: Cambridge University Press.

Wheelon, A. D., Short, N., & Townes, C. H. (2007). Low-frequency behavior of turbulence fluctuations at Mount Wilson Observatory. *The Astrophysical Journal Supplement Series*, *172*(2).

Whittle, P. (1953). The Analysis of Multiple Stationary Time Series. *Journal of the Royal Statistical Society: Series B (Methodological)*, 15: 125-139. https://doi.org/10.1111/j.2517-6161.1953.tb00131.x

Wu, J. (2009). Mitigation of GPS carrier phase multipath effects using empirical mode decomposition. In I. Staff (Ed.), *2009 International Conference on Information Engineering and Computer Science* (pp. 1–4). IEEE.

Wu, Z., & Huang, N. E. (2004). A study of the characteristics of white noise using the empirical mode decomposition method. *Proceeding of the Royal Society of London A*, *460*, 1597–1611.

Appendix 1: Illustration of the psd for Phase and Phase Differences

We simulated time series from Eq. (5) using the proposal of Michael (2021) to give the reader a better understanding of this bandwidth noise. The elevation was kept constant for the sake of simplicity. The time series generated (Fig.

9 bottom, left) is not unique but has the statistical characteristics necessary. We varied the frequencies between 0 and 2 Hz and set the length of the time series to 5000 samples, i.e. long enough to allow a saturation of the psd at low frequency for the parameter rad/sample chosen. We further assume rad/sample and added a WN component of standard deviation 0.1 m. The choice of these parameters follows the aim of simulating realistic psd from GPS SDs. The following comments can be made:

- Two parts can be identified in the psd of the phase (Eq. (5)) illustrated in Fig. 1 (left, magenta line): (1) a power law of -8/3 and (2) a saturation beyond the cutoff frequency leading to a WN at low frequency, i.e. a 0-slope.
- The expression for the psd of the phase difference is slightly different as the factor is multiplied by the Matérn psd (see Eq. (4)). This leads to a radical change in the shape of the psd (as shown in Fig. 9, left, blue line, and Fig. 9, right, for a more detailed explanation). A smooth transition between the saturation at low frequency and the slope of -8/3 at higher frequencies is seen. This transition starts at and is softer than in the usual Matérn psd. A -2 power law in the middle frequency band is sometimes interpreted as the interference pattern of the receiver (Ishimaru, 2017).

We note a very important property: the cutoff frequency is not affected by the additional sinus term and is – visually – the same for both psd (see Fig. 9, blue and magenta line). Similarly, an additional flicker noise that may come from an electronic component or a random walk present at low frequency will not affect the cutoff frequencies: only their determination will be made more challenging, as developed in the next section.

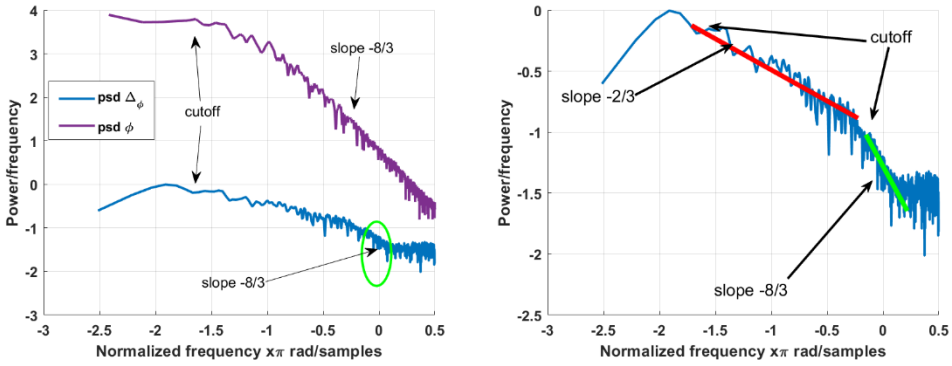

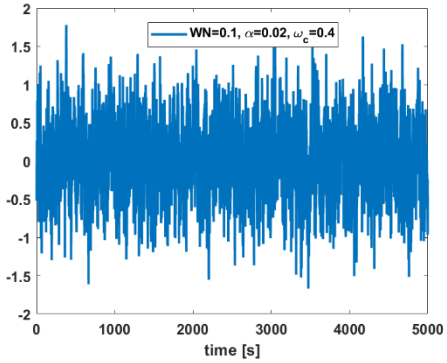

Fig. 9: The psd of phase difference given in dB/rad/samples. Top left: psd with a Matérn process (magenta) and psd for the phase difference (blue line). Right: illustration of the smooth transition between the two turbulent regimes at high and low frequency. Bottom left: a time series of 5000 samples at a data rate of 1 Hz with , (both given in rad/sample) and a WN factor of 0.1 m. All psd are presented in a loglog plot.

Appendix 2: The Whittle Maximum Likelihood Estimator

The maximum likelihood estimator performs poorly if the assumption of a strict long-range dependence is incorrect (i.e. in the presence of additional effects or frequencies) or for short samples (Sykulski et al., 2019). This situation is met here, due to the presence of the sinus term in the expression of the phase difference. Exact maximum likelihood inference can be performed for Gaussian data (Brockwell & Davis, 1991) by evaluating the aforementioned log-likelihood , with means the covariance matrix of the observations and the residuals vector after least-squares approximation. This procedure necessitates matrix inversions. They can be avoided using the Whittle estimator (Whittle, 1953), which aims to provide faster estimation with only a slight inaccuracy. In that case, the Whittle likelihood in its discretized form is given by , with the set of discrete Fourier frequencies, the continuous-time process spectral density and the periodogram . This estimator permits one to obtain the parameters of Matérn processes with a high trustworthiness, even for short samples

Appendix 3: The Empirical Mode Decomposition

Huang et al. (2005) developed the EMD to decompose a given time series into a set of components of different time scales called the IMFs. Combined with the Hilbert-Huang Transform, this decomposition provides a time-frequency-energy representation of a signal. A major field of applications of EMD is to denoise a signal (see e.g. Montillet et al., 2013 for an application to geodetic coordinate time series). The original temporal signal is a non-weighted combination of the IMF , being the residuals after decomposition: . Each IMF has a variance , corresponding to its mean energy. Regarding power-law noises, the first IMF is said to contain most of the WN component of the signal (see Fig. 10, left). The

variance of the other IMFs decreases linearly in a semi-log diagram regarding the IMF index (Fig. 10, right). The slope can be computed by regression and is directly related to the power law of the noise, also called Hurst exponent (see Flandrin et al., 2004). The IMF energy that does not lie on the line is associated with a "signal." This latter can simply be eliminated. In this contribution, we will make use of the 3 rule. Accordingly, we decompose the noise into 7 IMFs; we note that this number is rather empirical and left to the user's convenience, i.e. the methodology is similar if the noise is decomposed into more modes. We, furthermore:

- iteratively control whether to decide whether the i^{th} IMF should be excluded or not. is the standard error for the prediction of the regression line between , for which corresponds to a roughly 68 % prediction interval. The IMF energy that is not within the confidence interval of 3is considered to be a "signal," i.e. a multipath or any functional misspecifications or noise with a higher power law than the noise from which we wish to compute the cutoff frequencies.
- The filtered is finally computed as: , where depends on the remaining number of IMFs .

The EMD and variance analysis allow us, thus, to filter the power-law noises from additional unwanted effects, such as random-walk or flicker noise, coming from inaccuracies in the deterministic model, e.g. unmodelled additional periodic components.

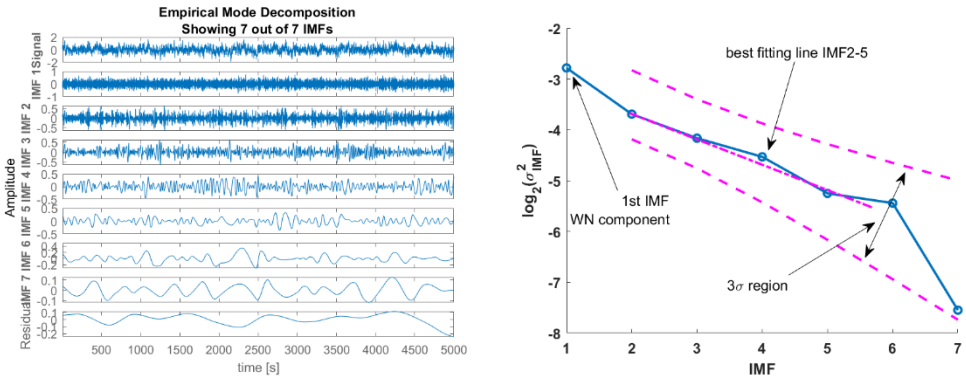

Fig. 10: left: the EMD of an exemplary signal corresponding to a SD residual. Right: the Hilbert–Huang transform and its log2 variance plot regarding the IMF of the decomposition.